Nanoscale Advances

ROYAL SOCIETY OF CHEMISTRY

COMMUNICATION

View Article Online
View Journal | View Issue

Cite this: *Nanoscale Adv.*, 2025, **7**, 6422

Received 18th June 2025
Accepted 25th August 2025

DOI: 10.1039/d5na00602c

rsc.li/nanoscale-advances

Scalable synthesis and optical tuning of $CsPbBr_3$ nanocrystal inks for dual-color anti-counterfeiting applications

Tianming Sun†, Yining Zhao,† Yujia Fan, Xiaoyu Guo, Zhexin Tang and Mingqing Wang *

We present a scalable, ambient-air synthesis of $CsPbBr_3$ perovskite nanocrystal (NC) inks with enhanced optical performance and environmental stability, enabled by post-synthetic surface modification using oleylamine (OAm). Systematic tuning of OAm concentration led to NCs with reduced particle size, improved crystallinity, and effective defect passivation, yielding a peak photoluminescence quantum yield (PLQY) of 93.1% and a prolonged carrier lifetime of 84.02 ns. These modified NCs exhibited significantly improved long-term structural stability compared to unmodified samples. Furthermore, halide exchange *via* iodine incorporation enabled controlled emission tuning from green to red. Dual-color emissive inks were digitally printed into high-resolution patterns on flexible substrates, which remained inconspicuous under visible light but displayed vivid fluorescence under UV illumination. This dual-mode visibility offers a secure and versatile platform for next-generation anti-counterfeiting technologies and information encryption, demonstrating the potential of perovskite NCs in advanced functional ink applications.

With the rapid growth of the global commodity economy and the expansion of market demands, consumer expectations have intensified. However, the proliferation of counterfeit goods has become a serious worldwide issue, undermining the rights of both consumers and legitimate businesses.[1] To combat counterfeiting, a range of technologies has been developed, including watermarking,[2] barcodes,[3] laser holography,[4] and fluorescent labelling.[5] These techniques have increased the technical threshold for forgery and provided essential protection for intellectual property. Among them, fluorescent anti-counterfeiting labels are currently the most widely adopted and technologically mature, especially in currency authentication systems.[6] Yet, traditional fluorescent materials are increasingly inadequate in meeting evolving demands for advanced security features.[7] In response, emerging luminescent materials—such as carbon dots,[8] semiconductor quantum dots,[9] and metal–organic frameworks (MOFs),[10,11] including those doped with rare-earth ions or organic dyes—have been explored. These materials offer improved optical properties and anti-counterfeiting reliability.[12] Nevertheless, their widespread adoption is hindered by complex synthesis procedures, high production costs, and integration challenges.

In this context, inorganic halide perovskite nanocrystals (NCs) have emerged as promising next-generation luminescent materials. Their tunable emission—achieved through size control, compositional engineering, and ion doping—coupled with exceptional properties such as high photoluminescence quantum yield (PLQY), narrow emission linewidths,[13–16] broad color tunability,[17] and superior charge-carrier mobility, makes them attractive candidates for anti-counterfeiting applications.

However, significant obstacles remain. The conventional hot-injection synthesis method requires elevated temperatures and inert environments, limiting scalability and reproducibility.[18] Furthermore, perovskites' ionic nature renders them chemically unstable, particularly under exposure to moisture and oxygen. A critical bottleneck is the drastic drop in PLQY when nanocrystals are transitioned from solution to solid state, primarily due to ligand desorption and accelerated ion migration, which leads to fluorescence quenching.[19] Therefore, developing a facile strategy to produce stable, highly luminescent $CsPbX_3$ NCs is vital for their practical implementation in next-generation anti-counterfeiting technologies.[20]

In this work, we report a rapid and scalable synthesis of $CsPbBr_3$ perovskite NCs inks using short-chain, low-boiling-point ligands and solvents. This approach enables precise control over the crystal structure while facilitating large-scale production. To further enhance the material properties, post-synthetic ligand modification was performed using the long-chain ligand oleylamine (OAm). Optimization of OAm concentration led to the formation of smaller nanocrystals with significantly improved optical and chemical stability, achieving a photoluminescence quantum yield (PLQY) of up to 93.1%.

Fig. 1 shows the XRD patterns of $CsPbBr_3$ NCs thin film samples modified with varying amounts of OAm. The small

UCL Institute for Materials Discovery, University College London, Roberts Building, Malet Place, London, WC1E 7JE, UK. E-mail: mingqing.wang@ucl.ac.uk

† These authors contributed equally to this work.

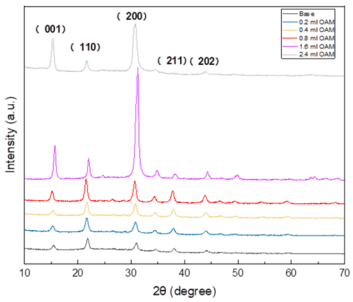

Fig. 1 XRD Patterns of $CsPbBr_3$ NCs modified with varying amounts of OAm.

crystallite size of $CsPbBr_3$ nanocrystals results in significant XRD peak broadening, complicating precise phase determination. After Rietveld refinement using GSAS II, the XRD peaks match well with the standard cubic perovskite phase with lattice parameter (a) of 5.87 Å (PDF 00-054-0752, ICDD), confirming the preservation of the expected perovskite crystal structure. Importantly, OAm addition did not induce any phase change. The intensity of the diffraction peaks increased with OAm content, indicating enhanced crystallinity, with the highest crystallinity observed at 0.8 mL of OAm. However, further increase in OAm led to a relative enhancement of the (200) peak intensity, suggesting a shift in crystal growth orientation at higher ligand concentrations. The calculated crystallite sizes decreased with increasing oleylamine (OAm) concentration, confirming the role of ligand modification in size control. Specifically, the crystallite size reduced from approximately 13.2 nm (unmodified) to 8.4 nm for samples treated with 1.6 mL of OAm.

The morphology and elemental composition of $CsPbBr_3$–OAm NCs were analyzed using scanning electron microscopy (SEM) and energy-dispersive X-ray spectroscopy (EDS). As shown in Fig. 2a, the Cs, Pb, and Br elements are uniformly distributed throughout the $CsPbBr_3$–OAm sample. The corresponding atomic ratio of Cs : Pb : Br, calculated from the weight percentages shown in Fig. 2b, is approximately 1 : 1.04 : 3.33. This is in close agreement with the ideal perovskite stoichiometry of $CsPbBr_3$, indicating good elemental composition. The slight excess of Br is likely due to the presence of surface ligands or halide-rich synthesis conditions.

For nanocrystals, crystal size plays a crucial role in determining their optical and electronic properties. Variations in size directly influence key parameters such as bandgap and the density of electronic and hole states. Fig. 3a shows the normalized UV-Vis absorption spectra of $CsPbBr_3$ NCs modified with varying amounts of OAm. A progressive blue shift of the absorption edge is observed with increasing OAm concentration, indicating a decrease in nanocrystal size due to quantum confinement effects. This behavior suggests that higher OAm content effectively limits crystal growth during synthesis, likely by capping active growth sites and passivating surfaces.

Transmission electron microscopy (TEM) images further corroborate this trend. As shown in Fig. 3b, the unmodified $CsPbBr_3$ NCs exhibit aggregated particles with irregular and poorly defined morphologies, including a mix of quasi-spherical and distorted shapes, indicative of incomplete surface passivation and uncontrolled growth. In contrast, Fig. 3c shows that the $CsPbBr_3$ NCs synthesized with 1.6 mL OAm display improved dispersity, with well-defined, faceted rectangular or cuboidal shapes and uniform size distribution. These observations confirm that OAm not only modulates nanocrystal growth and morphology but also contributes to improved crystallinity and surface quality, in line with the optical trends observed in the UV-Vis spectra.

Fig. 4a shows the photoluminescence (PL) spectra of $CsPbBr_3$–OAm nanocrystals (NCs), while Table 1 summarizes their corresponding photoluminescence quantum yield (PLQY) values. As the OAm concentration increases, the PL intensity gradually increases. The PLQY exhibits a trend of first increasing and then decreasing, with a maximum value observed at an OAm concentration of 1.6 mL. This behavior is attributed to the dual role of OAm. At moderate concentrations, OAm effectively passivates surface defects, enhancing emission by suppressing non-radiative recombination pathways. Surface defects typically act as non-radiative centers, where excited carriers recombine without photon emission, thereby lowering overall PL efficiency. By passivating these defects, OAm reduces

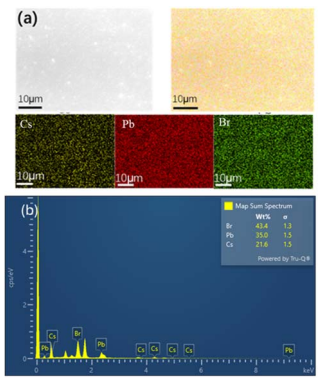

Fig. 2 (a) SEM image and corresponding elemental mapping of Cs, Br, and Pb showing uniform spatial distribution. (b) EDS spectrum confirming Cs, Pb, and Br with their respective weight ratio.

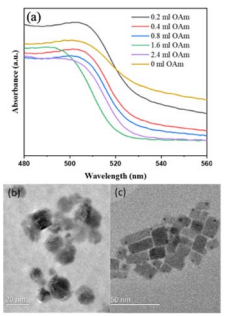

Fig. 3 (a) Normalized absorption spectra of $CsPbBr_3$ NCs synthesized with different volumes of OAm. (b) TEM image of $CsPbBr_3$ NCs without OAm. (c) TEM image of $CsPbBr_3$ with 1.6 mL OAm.

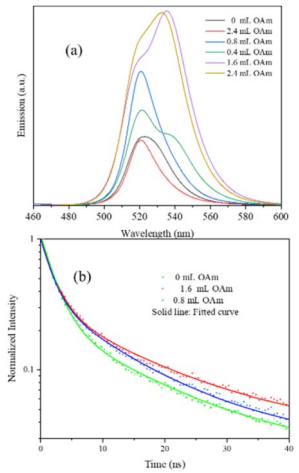

Fig. 4 (a) PL and(b) TRPL of OAm Modified $CsPbBr_3$ NCs.

Table 1 The PLQY of OAm Modified $CsPbBr_3$ NCs

Added OAm (mL)	0	0.2	0.4	0.8	1.6	2.4
PLQY (%)	48.4	68.7	72.6	85.5	91.3	26.8

non-radiative losses and promotes radiative recombination, resulting in stronger PL intensity and higher PLQY. However, at higher OAm concentrations, excessive ligand coverage introduces steric hindrance and may lead to an excess of uncoordinated Pb atoms on the surface, ultimately diminishing the emission efficiency.

Fig. 4b presents the time-resolved photoluminescence (TRPL) curves of OAm-modified $CsPbBr_3$ nanocrystals (NCs). As shown, the PL decay rate decreases with increasing OAm content. The sample modified with 1.6 mL of OAm exhibits the slowest decay rate, indicating the highest photoluminescence efficiency and the lowest non-radiative recombination. This suggests that surface defects have been effectively passivated in this sample.

Details of the TRPL curve fitting and lifetime calculation are provided in the SI. The average photoluminescence lifetime of $CsPbBr_3$–OAm (1.6 mL) NCs is 84.02 ns, significantly longer than that of the unmodified $CsPbBr_3$ NCs (44.95 ns). This extension in lifetime confirms that ligand modification effectively reduces non-radiative recombination, likely due to a decrease in surface defect density facilitated by OAm passivation.

To evaluate stability, the crystal structure of the samples was monitored over time. As shown in Fig. S1, the XRD pattern of unmodified $CsPbBr_3$ NCs shows the emergence of a diffraction peak at 12.5° after two months of storage, indicating structural degradation. In contrast, $CsPbBr_3$–OAm NCs maintain their structural integrity, demonstrating that OAm significantly improves the long-term stability of the nanocrystals. To better evaluate the long-term performance required for real-world applications, future work will focus on extended aging studies under more realistic environmental conditions, including exposure to humidity, light, and thermal cycling.

Fluorescent inks with tunable emission wavelengths offer significant advantages for anti-counterfeiting and information encryption. By adjusting the emission properties through compositional tuning, such inks can produce unique multicolor fluorescent patterns that are difficult to replicate, thereby enhancing security features in documents, packaging, and currency. Moreover, wavelength-selective inks enable multilevel encryption, where information remains hidden under normal lighting conditions but becomes visible under specific excitation wavelengths—adding an extra layer of protection against counterfeiting and unauthorized access.

To achieve red emission, iodine substitution was performed on $CsPbBr_3$ NCs by partially replacing Br^- with I^-. Specifically, 300 μL, 450 μL, 600 μL, and 750 μL of a 4 M LiI ethanol solution were added to 10 mL of $CsPbBr_3$ NC dispersion. Upon addition, the solution gradually changed colour from green to red, indicating successful halide exchange.

As shown in Fig. 5a, PL measurements confirm that increasing iodine content leads to a red-shift in the emission peak, validating iodine substitution as an effective strategy for tuning the optical properties of perovskite NCs. The anti-counterfeiting pattern printed on a PI substrate using both green and red emissive inks exhibits clear and vivid features under UV light. As shown in Fig. 5b, the pattern remains nearly invisible under visible light, closely matching the background colour of the substrate. However, under UV illumination, the pattern becomes highly visible—displaying bright green and sharp red fluorescence—forming a distinctive, multicolour image that is difficult to replicate. This dual-mode visibility, depending on the illumination source, provides a robust and reliable means of authentication. The unique fluorescence signatures offer a secure verification mechanism, making these perovskite-based inks highly suitable for advanced anti-counterfeiting applications.

This work presents a rapid and scalable approach for producing $CsPbBr_3$ NCs inks with enhanced luminescent

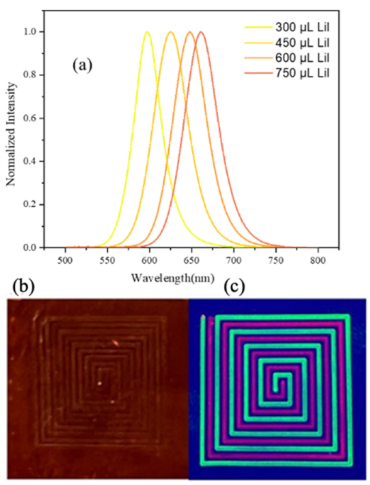

Fig. 5 (a) PL spectra of $CsPbBr_3$–LiI nanocrystals with varying LiI concentrations. (b) Printed patterns observed under visible light. (c) Corresponding photoluminescent patterns under UV illumination.

properties and stability through ligand engineering. The introduction of 1.6 mL OAm optimized nanocrystal size, improved crystallinity, and passivated surface defects—resulting in a peak PLQY of 93.1% and significantly prolonged carrier lifetimes, as confirmed by TRPL analysis. OAm modification also improved long-term structural stability, minimizing aggregation and providing protection from environmental degradation. Furthermore, halide exchange *via* iodine substitution enabled precise tuning of emission wavelengths, facilitating the fabrication of red- and green-emissive inks. Using a Sonoplotter, dual-color inks were printed into high-resolution patterns on flexible substrates. These patterns, invisible under ambient light but highly emissive under UV illumination, offer a robust and multi-layered anti-counterfeiting strategy. The ability to integrate wavelength-tunable, luminescent perovskite inks with digital printing techniques provides a promising platform for next-generation security applications in currency, branded products, and confidential documentation.

Author contributions

Tianming Sun and Yining Zhao contribute equally on the work. All authors have given approval to the final version of the manuscript.

Conflicts of interest

The authors declare no competing financial interests.

Data availability

The raw data files are available upon request from the corresponding authors.

Supplementary information: All scientific data has been reported in the main manuscript and SI. See DOI: **https://doi.org/10.1039/d5na00602c**.

Acknowledgements

The authors would like to acknowledge the financial support from the European Commission supported this work under the H2020 HI-ACCURACY project (grant agreement ID: 862410).

Notes and references

1 W. Ren, G. Lin, C. Clarke, J. Zhou and D. Jin, *Adv. Mater.*, 2020, **32**, 1901430.
2 M. Yang, Y. Liu and X. Jiang, *Chem. Soc. Rev.*, 2019, **48**, 850–884.
3 J. Pan, X. Sun, S. Chu, A. Abraham and B. Yan, *Eng. Appl. Artif. Intell.*, 2021, **97**, 104049.
4 M. Carstensen, X. Zhu, O. Iyore, N. Mortensen, U. Levy and A. Kristensen, *ACS Photonics*, 2018, **5**, 1665–1670.
5 J. Wu, Q. Liu, P. Gao, J. Wang, Y. Qi, Z. Li, *et al.*, *Nanomaterials*, 2023, **13**, 2457.
6 Z. Song, T. Lin, L. Lin, S. Lin, F. Fu, X. Wang, *et al.*, *Angew. Chem., Int. Ed.*, 2016, **55**, 2773–2777.
7 X. Yu, H. Zhang and J. Yu, *Aggregate*, 2021, **2**, 20–34.
8 S. Choi, J. Drese and W. Jones, *ChemSuschem*, 2009, **2**, 796–854.
9 Y. Liu, F. Han, F. Li, Y. Zhao, *et al.*, *Nat. Commun.*, 2019, **10**, 2409.
10 W. Liu, G. Liu, X. Zhu, X. Han, A. Lu, *et al.*, *New J. Chem.*, 2022, **46**, 8062–8068.
11 M. Li, G. Ren, W. Yang and Q. Pan, *CrystEngComm*, 2023, **25**, 704–714.
12 J. Andres, R. Hersch, J. Moser and A. Chauvin, *Adv. Funct. Mater.*, 2014, **24**, 5029–5036.
13 L. Protesescu, S. Yakunin, M. Bodnarchuk, F. Krieg, R. Caputo, *et al.*, *Nano Lett.*, 2015, **15**, 3692–3696.
14 V. Ravi, G. Markad and A. Nag, *ACS Energy Lett.*, 2016, **1**, 665–671.
15 Z. Tan, R. Moghaddam, M. Lai, P. Docampo, R. Higler, *et al.*, *Nat. Nanotechnol.*, 2014, **9**, 687–692.
16 S. Veldhuis, P. Boix, N. Yantara, M. Li, T. Sum, N. Mathews, *et al.*, *Adv. Mater.*, 2016, **28**, 6804–6834.
17 J. Yu, D. Kim, G. Baek, B. Lee, E. Jung, *et al.*, *Adv. Mater.*, 2015, **27**, 3492–3500.
18 C. Stoumpos and M. Kanatzidis, *Adv. Mater.*, 2016, **28**, 5778–5793.
19 H. Chen, Y. Li, B. Zhao, J. Ming and D. Xue, *Nano Futures*, 2022, **6**, 012001.
20 T. Jeon, S. Kim, J. Yoon, J. Byun, H. Hong, *et al.*, *Adv. Energy Mater.*, 2017, **7**, 1602596.